Composite Structures 160 (2017) 516–528

Contents lists available at ScienceDirect

Composite Structures

journal homepage: www.elsevier.com/locate/compstruct

Modelling and characterisation of dynamic behaviour of short-fibre-reinforced composites

M. Nciri [a,b], D. Notta-Cuvier [a,*], F. Lauro [a], F. Chaari [a], Y. Maalej [c], B. Zouari [b]

[a] University of Valenciennes and Hainaut Cambrésis (UVHC), LAMIH UMR CNRS 8201, 59313 Valenciennes, France
[b] National Engineering School of Sfax (ENIS), LA2MP, B.P. W3038 Sfax, Tunisia
[c] University of Tunis El Manar, ENIT, MAI (LR11ES19), 1002 Tunis, Tunisia

ARTICLE INFO

Article history:
Received 14 June 2016
Revised 13 September 2016
Accepted 19 October 2016
Available online 21 October 2016

Keywords:
Short fibre reinforced composites
Viscoelastic–viscoplastic behaviour
Distributed fibre orientation

ABSTRACT

This study proposes a constitutive model of viscous behaviour of short-fibre reinforced composites (SFRC) with complex distributions of fibre orientations and for a wide range of strain rates. The model is based on an additive decomposition of the state potential for the computation of composite macroscopic behaviour. Thus, the composite material is seen as the assembly of a matrix medium and several linear elastic fibre media. The division of short fibres into several families means that complex distributions of orientation or random orientation can be easily modelled. The matrix behaviour is strain-rate sensitive, i.e. viscoelastic and/or viscoplastic. Viscoelastic constitutive laws are based on a generalised linear Maxwell model and the modelling of the viscoplasticity is based on an overstress approach. The accuracy of the model is assessed for the case of polypropylene reinforced with short glass fibres. Matrix material parameters are identified from experimental tests carried out at several loading rates. Distributions of fibre orientation are characterised by micro-computed tomography. Comparisons between numerical and experimental responses in different loading directions and under different strain rates demonstrate the efficiency of the model.

1. Introduction

Short-fibre-reinforced composites (SFRC) are commonly used in a variety of engineering applications, including automotive and aerospace industry. The effectiveness of these materials is mainly due to high stiffness to density ratio, in particular, resulting from reinforcement with high-rigidity fibres. Today, the use of SFRC is progressively extended to parts possibly subjected to severe loading conditions (e.g. crash...), characterised by high strain rates. Then, it becomes crucial to have access to a reliable and accurate modelling of SFRC's behaviour that can take strain-rate sensitivity into account, in addition to other specificities.

SFRC are generally processed by injection moulding. In that case, the fibres diluted in the matrix follow distributions of orientation that depend on process parameters and highly influence composite behaviour. In fact, SFRC macroscopic behaviour depends on numerous microscopical interferent phenomena that must be taken into account in behaviour models. In particular, complex matrix behaviour, load transfer at fibre/matrix interface and damage mechanisms of constituents or of the interface (i.e fibre/matrix debonding) have to be considered in constitutive modelling. An important point is that all these phenomena strongly depend on local fibre characteristics (e.g. orientation with respect to macroscopic loading direction). Yet, knowing the actual local reinforcement configuration is not so easy and deep investigations have to be done, for instance by using micro-tomography [1,2].

Thermoplastic matrices generally exhibit a rate-dependent behaviour at all stages of deformation. Dealing with various approaches can be considered: Viscoelasticity, Viscoplasticity and Viscoelasticity/viscoplasticity [3–7]. Moreover, during tensile tests, non-uniform plastic strain and strain-rate fields are generally developped even at moderate strain level. In that context Digital Image Correlation (DIC) technique is a more and more widespread method used to acquire local value of displacement/strain fields throughout loadings. The captured heterogeneity of mechanical fields is then used to identify behaviour law, based on several methods [8–10]. Among available techniques, Lauro et al. have developped the *SEÈ* method [11]. Local values of stresses, strains and strain-rates are used to build a surface behaviour called the *SEÈ* surface where parameters of viscoelastic and/or viscoplastic behaviour law can be determined.

* Corresponding author.
E-mail address: delphine.notta@univ-valenciennes.fr (D. Notta-Cuvier).

http://dx.doi.org/10.1016/j.compstruct.2016.10.083
0263-8223/

Computation of macroscopic stress–strain relationship of SFRC is treated in the literature mainly on the basis of micro-mechanical approaches. Among them one may cite: direct finite element (FE) analysis on representative cells of the microstructure [12], mean-field homogenization (MFH) techniques and the asymptotic or mathematical theory of homogenization [13,14]. Mean-field methods were first proposed for composites with linear elastic constituents, relying on the exact solution of Eshelby [15] for an ellipsoidal inclusion embedded in an infinite matrix. Most common approaches are Mori and Tanaka [16], self-consistent [17,18] and double inclusion [19] schemes. Such models provide an estimation of the effective stress–strain relationship, in terms of volume averaged mechanical fields within the phases.

More recently these schemes have been extended to non-linear behaviour of one or more of constituents based on the linearisation of the local constitutive equations and the definition of uniform reference properties (e.g. secant [20,21], tangent [22] and affine [23] methods).

Viscoelasticity of SFRC has been introduced within the homogenisation technique using the correspondance principle, according to which constitutive equations in the time domain are recast into a linear elastic form into the Laplace domain [24,25]. After homogenisation in the Laplace space, the effective properties are found by the inverse transform. Masson and Zaoui [26] and Pierard and Doghri [27] used this approach to model linearised elasto-viscoplastic composites. The main drawback of this approach is its numerical cost related to the inversion of the Laplace transform.

Compared to viscoelastic or elasto-(visco) plastic behaviour modelling of thermoplastics, the modelling of viscoelastic–visco plastic (VE–VP) short-fibre reinforced composites has received little attention up to now and even less in case of distributed orientations, typical of injection moulding process. In addition to limitations dealing with constituents' behaviour laws, inclusion-type problems can become very difficult to handle in the case of reinforcement with non-aligned short fibres. To overcome this difficulty, Doghri and Tinel [28] have developed a double step homogenisation procedure. In a first step, a two-phase "pseudo-grain" constituted of the matrix material reinforced with identical and aligned fibres is homogenised. The second step then consists in the homogenisation of all pseudo-grains to compute mechanical properties at the representative elementary volume scale, taking all orientations of the fibres are taken into account.

All these contributions show that the difficulty of implementing homogenisation based models for SFRC increases significantly as the behaviour of constituents and fibres orientation distribution become more complex. To author's knowledge, no behaviour model enables today to deal with VE-VP matrix reinforced with fibres with complex distributions of orientation. Therefore, it is very interesting to consider models of composite behaviour at an intermediate scale between very complex homogenisation approaches and often inaccurate purely phenomenological descriptions. In that context, an alternative was recently developped based on the additive decomposition of the composite thermodynamic potential. The composite is thus seen as the assembly of a matrix medium and several media of embedded fibres. The deformation gradient, applied to the composite as a whole, and its multiplicative decomposition implicitly link the media. Nedjar [29] used this approach for viscoelastic materials, assuming that fibres carry load only in tension. Klinkel et al. [30] showed it can be theoretically applied to non-linear elasto-plastic behaviour for the matrix and the fibres. Nevertheless, there is no practical application of their implementations in the analysis of a short-fibre-reinforced material's behaviour. More recently, Notta-Cuvier et al. [31] used this approach to deal with rate-independent elastoplastic SFRC behaviour. A main asset of this approach is its adaptability to all kinds of reinforcement characteristics (orientation and geometrical properties) and matrix behaviour while keeping the implementation relatively easy.

The present work deals with the modelling of SFRC's behaviour when subjected to severe loading conditions, in particular at high strain rates. The approach developped by Notta-Cuvier et al. [31] is therefore extended here to viscous SFRC behaviour. To this end, the matrix behaviour is modelled using a coupled VE-VP scheme. Complex distributions of fibre orientation are considered, leading to an accurate representation of the actual reinforcement orientations. Thus, the coupled influence of strain rate and anisotropy of SFRC behaviour can be modelled.

The paper is organised as follows. The developed constitutive equations of the coupled viscoelastic–viscoplastic response of composite material are exposed in Section 2. In Section 3, the characterisation of the matrix material behaviour is performed based on Dynamic Mechanical Analysis as well as compression and tensile tests at different loading rates. The predicted behaviour of the matrix material is then evaluated by comparison with experimental tensile tests at a wide range of strain rates. Section 4 deals with the characterisation of fibre distribution of orientation using micro-computed tomography. The characterisation of SFRC's behaviour is then presented and the developped constitutive model is validated in tension, under a wide range of strain-rate. It is worth mentioning that the current characterisation and validation work will be extended in a further part of this project, namely with loading/unloading tests.

2. Constitutive model

The composite material is made of short fibres assumed to be uniformly dispersed in the matrix medium. For modelling purposes, the composite is seen as the assembly of a matrix medium and several fibre media (or "families"). Fibres with the same orientation, geometrical characteristics and material behaviour are grouped into a same family. Each fibre family is characterised by its own orientation vector, expressed in the global coordinate system (i.e. linked to the matrix), and volume fraction, computed according to actual fibre distribution of orientations and geometrical characteristics (note that in the present paper, all fibres have the same geometrical characteristics but distributions of orientation are considered). A fundamental assumption is that fibres carry load only in their direction of orientation. Therefore, the deformation gradient tensor associated to a given fibre family is the projection of the global deformation gradient tensor (i.e. applied to the composite) along fibre orientation. Behaviour of fibre families and matrix material are successively computed before the 3D-stress state of the composite material is determined via an additive decomposition of the specific free energy potential, as described hereafter.

2.1. Stress state of the matrix material

In order to predict the rate-dependent behaviour of thermoplastic matrix, a coupled viscoelastic (VE)-viscoplastic (VP) scheme is considered here. A first assumption is that the matrix total strain, ε, is subdivided into VE and VP parts, so that:

$$\varepsilon = \varepsilon^{ve} + \varepsilon^{vp} \tag{1}$$

It is worth noting that this decomposition is valid in the framework of small deformation, which is consistent with composite behaviour. Although unreinforced polymeric matrix can axhibit high level of deformation, this assumption remains valid when dealing with reinforced matrix.

The viscoelastic part of the response is modelled using the Generalized Maxwell model with a finite number of Maxwell elements arranged in parallel with a linear elastic Hooke element. It is to note here that the choice of a linear viscoelastic model is considered to be appropriate in the case of composites with relatively high volume fraction of reinforcement. However, the modelling scheme allows its adaptativity to all kind of matrix model of behaviour. If needed, the model can therefore theoretically be extended to nonlinear viscoelastic constitutive laws. A return mapping algorithm is implemented with a VE predictor step, followed if necessary by a VP corrector step. It is worth noting that physical basis are associated to this strain decomposition. Indeed, several micromechanical observations tend to show that crystalline lamellae and amorphous chains, present in thermoplastic polymer microstructure, obey VE and VP behaviour, respectively, and are assembled in series (thus following a Reuss model [32]). The Cauchy stress tensor of the matrix, $\sigma_M(t)$, is linearly related, at an instant t, to the history of VE strain, ε^{ve}, via Boltzmann's hereditary integral:

$$\sigma_M(t) = \int_{-\infty}^{t} R^{ve}(t-\zeta) : \frac{\partial \varepsilon^{ve}(\zeta)}{\partial \zeta} d\zeta \tag{2}$$

where R^{ve} is the fourth order relaxation tensor expressed by:

$$R^{ve}(t) = 2G(t)I^{dev} + 3K(t)I^{vol} \tag{3}$$

I^{vol} and I^{dev} are volumetric and deviatoric operators defined by: $I^{vol} = \frac{1}{3}1 \otimes 1$ and $I^{dev} = I - I^{vol}$, where 1 and I are respectively the second and the fourth order identity tensors. $G(t)$ and $K(t)$ are shear and bulk relaxation functions, respectively, expressed in the form of Prony series:

$$\begin{aligned} G(t) &= G_\infty + \sum_{i=1}^{N} G_i exp\left(-\frac{t}{\tau_i^d}\right) \\ K(t) &= K_\infty + \sum_{i=1}^{N} K_i exp\left(-\frac{t}{\tau_i^v}\right) \end{aligned} \tag{4}$$

where N is the number of Maxwell elements, τ_i^d, τ_i^v, G_i and $K_i, i \in \{1,\ldots,N\}$, are respectively the deviatoric and volumetric relaxation times and their corresponding shear and bulk moduli. G_∞ and K_∞ are respectively the long-term elastic and shear moduli. According to definitions given by Ohkami and Ichikawa [33], the deviatoric and volumetric relaxation times are expressed as follows:

$$\tau_i^d = \frac{\eta_i^d}{G_i}, \qquad \tau_i^v = \frac{\eta_i^v}{K_i} \quad \forall i \in \{1,\ldots,N\} \tag{5}$$

where η_i^d and η_i^v are the deviatoric and volumetric viscous coefficients. The VE strain tensor $\varepsilon^{ve}(t)$ is divided, in the same way, into deviatoric, $\varepsilon_{dev}^{ve}(t)$, and dilatational, $\varepsilon_H^{ve}(t)$, parts:

$$\varepsilon^{ve}(t) = \varepsilon_{dev}^{ve}(t) + \varepsilon_H^{ve}(t)1 \tag{6}$$

The deviatoric, $S_M(t)$, and dilatational, $\sigma_{M,H}(t)$, parts of the stress tensor are therefore defined by:

$$\begin{aligned} S_M(t) &= S_{M_\infty}(t) + \sum_{i=1}^{N} S_{M_i}(t) \\ \sigma_{H,M}(t) &= \sigma_{H,M_\infty}(t) + \sum_{i=1}^{N} \sigma_{H,M_i}(t) \end{aligned} \tag{7}$$

where

$$\begin{aligned} S_{M_\infty}(t) &= 2G_\infty \epsilon_{dev}^{ve}(t) \\ \sigma_{H_\infty}(t) &= 3K_\infty \epsilon_H^{ve}(t) \end{aligned} \tag{8}$$

$$\begin{aligned} S_{Mi}(t) &= 2G_i \int_{-\infty}^{t} exp\left(\frac{\zeta - t}{\tau_i^d}\right) \frac{\partial \epsilon_{dev}^{ve}(\zeta)}{\partial \zeta} d\zeta \\ \sigma_{H,M_i}(t) &= 3K_i \int_{-\infty}^{t} exp\left(\frac{\zeta - t}{\tau_i^v}\right) \frac{\partial \epsilon_H^{ve}(\zeta)}{\partial \zeta} d\zeta \end{aligned} \tag{9}$$

In addition to linear viscoelastic behaviour, matrix material can show a non-linear plastic behaviour, possibly strain-rate dependent, i.e. viscoplastic. Matrix behaviour is also pressure sensitive, i.e. sensitive to the nature of loading (e.g., tension, compression..) and non-isochoric in the plastic domain. Consequently, the framework of non-associated viscoplasticity is considered in this work, following Perzyna model [34]. The pressure dependency of the viscoplastic flow is introduced by Raghava yield surface [35]. Viscoplastic flow occurs as soon as the first invariant, I_1 (Eq. (10a)), and the second invariant, I_2 (Eq. (10b)), of the matrix Cauchy stress tensor reach a critical combination given by the yield surface expression (Eq. (11)).

$$I_1 = tr(\sigma_M(t)) \tag{10a}$$

$$I_2 = \frac{1}{2} S_M(t) : S_M(t) \tag{10b}$$

$$f(I_1, I_2, R) = \frac{(\eta - 1)I_1 + \sqrt{(\eta - 1)^2 I_1^2 + 12\eta I_2}}{2\eta} - \sigma_t - R(\kappa) \geqslant 0 \tag{11}$$

In previous expression, the hydrostatic pressure dependency parameter, η, is defined by the ratio between the quasi-static initial yield stresses in compression and tension, σ_{comp} and σ_t, respectively, so that $\eta = \sigma_{comp}/\sigma_t$. $R(\kappa)$ is the isotropic hardening function that must be identified in tension for the considered polymeric material. It is important to note that all types of hardening laws can be considered in the present behaviour model. Here, hardening law given by Eq. (12) will be considered.

$$R(\kappa) = h_1 exp(h_2 \kappa^2)(1 - exp(-h_3 \kappa)) \tag{12}$$

where h_1, h_2 and h_3 are material parameters and κ is the equivalent viscoplastic strain defined by:

$$\kappa = \int_t \sqrt{\frac{2}{3} \dot{\varepsilon}^{vp} : \dot{\varepsilon}^{vp}} dt \tag{13}$$

with $\dot{\varepsilon}^{vp}$ the viscoplastic strain rate tensor. The non symmetric and non isochoric plastic flow of the polymeric matrix is modelled by a hyperbolic viscoplastic dissipation potential [36], defined by:

$$\psi_M^{vp}(I_1, I_2) = \sqrt{3I_2 + \frac{1}{3}\left(a^+ \langle I_1 \rangle^2 + a^- \langle -I_1 \rangle^2\right)} \tag{14}$$

where the symbol $\langle . \rangle$ is the Macauley braket defined by $\langle x \rangle = \frac{(x+|x|)}{2}$, for any scalar x. a^+ and a^- are volume variation parameters under positive and negative hydrostatic pressure, respectively. In the framework of non-associated viscoplasticity, $\dot{\varepsilon}^{vp}$ is derived from the viscoplastic potential of dissipation, ψ_M^{vp}, and expressed by the normality rule in terms of the viscoplastic multiplier rate, $\dot{\lambda}$, as follows:

$$\dot{\varepsilon}^{vp} = \dot{\lambda} \frac{\partial \psi_M^{vp}}{\partial \sigma_M} = \dot{\lambda} n \tag{15}$$

where n is the viscoplastic flow direction tensor. Given the expression of ψ_M^{vp}, (14), the expression of the viscoplastic strain rate tensor becomes:

$$\dot{\varepsilon}^{vp} = \dot{\lambda} \frac{\frac{3}{2} S_M + \frac{1}{9}(a^+ \langle I_1 \rangle + a^- \langle -I_1 \rangle) I}{3I_2 + \frac{1}{27}\left(a^+ \langle I_1 \rangle^2 + a^- \langle -I_1 \rangle^2\right)} \tag{16}$$

The viscoplastic multiplier rate, $\dot{\lambda}$, is calculated here using the approach of overstress based viscoplasticity. According to the latter theory, the static yield surface, f (Eq. (11)), is extended to a dynamic yield surface, F^{vp}, defined as follows [34]:

$$F^{vp}(I_1, I_2, R, \dot{\kappa}) = \frac{(\eta-1)I_1 + \sqrt{(\eta-1)^2 I_1^2 + 12\eta I_2}}{2\eta} - (\sigma_t + R(\kappa)) - \sigma^{vp} \tag{17}$$

where σ^{vp} is the viscous overstress. As postulated in Perzyna's model [34], this overstress is defined as follows:

$$\sigma^{vp} = (\sigma_t + R(\kappa))\left(\frac{\dot{\kappa}}{\dot{\kappa}_0}\right)^m \tag{18}$$

where m and $\dot{\kappa}_0$ are the strain rate sensitivity and viscosity parameters, respectively. $\dot{\kappa}$ is the equivalent viscoplastic strain-rate, defined by:

$$\dot{\kappa} = \sqrt{\frac{2}{3}\dot{\varepsilon}^{vp} : \dot{\varepsilon}^{vp}} = \dot{\lambda}\sqrt{\frac{2}{3}n : n} \tag{19}$$

The standard Kuhn-Tucker loading/unloading conditions are then applied to the dynamic yield surface (i.e., $F^{vp} \leq 0, \dot{\lambda} \geqslant 0$, $\dot{\lambda}F^{vp} = 0$) for the determination of the viscoplastic multiplier.

2.2. Stress state of fibre media

In SFRC, the load applied to the polymeric matrix is transferred to embedded fibres through the interface. Due to relatively high aspect ratio of fibres, each fibre family is assumed to carry load only in its axis direction, i.e. to behave unidimensionally. Moreover, as it is very likely that the composite fails before the stress applied to a fibre reaches its initial yield stress, fibre behaviour is assumed to remain linear elastic. As already stated, the presence of fibres with variable characteristics in the composite material is modelled by the coexistence of N_{fam} families. Each family i ($i \in \{1, \ldots, N_{fam}\}$) is characterised by its elastic properties (Young modulus E_F^i), its vector of orientation in global coordinates system, $\vec{a}^i$, and therefore matrix of orientation, A^i, defined by $A^i = \vec{a}^i \otimes \vec{a}^i$, i.e. $A^i_{kl} = a^i_k \otimes a^i_l, \forall k, l$, its geometric properties (i.e., diameter and length) and its volume fraction, v_F^i, so that $\sum_{i=1}^{N_{fam}} v_F^i = v_F = 1 - v_M$. v_F and v_M are respectively the total volume fraction of fibres and matrix in the composite material.

The computation of 1D fibre axial stress, $\sigma_F^{0\,i}$, is based on a formulation that is consistent with a local iso-strain state between the fibres and the matrix, in the direction of fibre axis [31,37,38]. The fibre tensor of deformation gradient, F_F^i, is defined as the projection of the total deformation gradient tensor, F, applied to the composite material, in the direction of fibre orientation (20).

$$F_F^i = FA^i \quad \forall i \in \{i, \ldots, N_{fam}\} \tag{20}$$

The right Cauchy-Green tensors of the composite, C, and fibre families, C_F^i, are defined by Eq. (21) and are therefore linked by the relation (22).

$$C = F^T F \quad and \quad C_F^i = F_F^{i^T} F_F^i \quad \forall i \in \{i, \ldots, N_{fam}\} \tag{21}$$

$$C_F^i = A^i C A^i \quad \forall i \in \{i, \ldots, N_{fam}\} \tag{22}$$

By construction, each tensor C_F^i has a unique eigenvalue different from zero, called λ_F^i, with associated eigenvector a^i. λ_F^i actually stands for the square of the ratio of the fibres current length by initial length. As a consequence, with the small strain assumption, the 1D Hencky strain of the fibres, $\varepsilon_F^{0\,i}$, is simply expressed from λ_F^i as follows:

$$\varepsilon_F^{0\,i} = \frac{1}{2} ln\left(\lambda_F^i\right) \quad \forall i \in \{i, \ldots, N_{fam}\} \tag{23}$$

A modified shear lag model is then used to compute average fibre axial stress, $\sigma_F^{0\,i}$. This model is based on initial work by Bowyer and Bader [39] and has been then extended to cases of complex fibre orientations, as described in details by Notta-Cuvier et al. [31]. According to this approach, the average 1D-stress state of each fibre family, $\sigma_F^{0\,i}, \forall i$, can be computed using Eq. (24). It can be noted that particular cases where fibres have different elastic properties (i.e. different values of E_F^i) can be dealt with and that the fibres response under compression is assumed to be the same as under tension (i.e. buckling is neglected) [31].

$$\begin{cases} \sigma_F^{0,i} = \varepsilon_F^{0,i}\left(1 - \frac{E_F^i r^i}{2L^i \tau^i}\left|\varepsilon_F^{0,i}\right|\right)E_F^i & \text{if} \left|\varepsilon_F^{0,i}\right| \leqslant \frac{L^i \tau^i}{E_F^i r^i} \\ \sigma_F^{0,i} = sign\left(\varepsilon_F^{0,i}\right)\frac{L^i \tau^i}{2r^i} & \text{otherwise} \end{cases} \tag{24}$$

where L^i and r^i are fibre length and radius, respectively, and τ^i is the interfacial shear strength for fibre family $i, \forall i \in [1, \ldots, N_{fam}]$. In addition to isostrain condition in fibre axis direction, quasi iso-stress states are assumed between the fibres and the matrix material in transverse and shear directions with respect to fibre axis. More precisely, fibre stresses in those directions are assumed to be equal to those of a fictitious purely viscoelastic material (with viscoelastic parameters of the matrix material), in accordance with the well-known principle of lower bound assumption. The expression of 3D stress tensor of fibre family i, σ_F^i, is therefore expressed in the global coordinate system by:

$$\sigma_F^i = T^i \begin{bmatrix} \sigma_F^{0,i} & \sigma_{M12}^{0,i} & \sigma_{M13}^{0,i} \\ \sigma_{M12}^{0,i} & \sigma_{M22}^{0,i} & \sigma_{M23}^{0,i} \\ \sigma_{M13}^{0,i} & \sigma_{M23}^{0,i} & \sigma_{M33}^{0,i} \end{bmatrix} T^{i^{-1}} \quad \forall i \tag{25}$$

where T^i is the transition matrix from the coordinate system related to the fibre family i to the global one; $\sigma_{Mkl}^{0,i}, k, l \in \{1, 2, 3\}$, are stress components of the purely viscoelastic "matrix" material, expressed in the coordinate system of fibre family i.

2.3. Stress state of the composite material

Once 3D stress tensors of the matrix material and all fibre families are computed, the composite stress tensor can be determined as a combination of the contribution of all fibre and matrix media [31]. Indeed, the state potential of the composite material, here the Helmholtz free energy, is assumed to be additively split into a part specific to the matrix medium and other parts specific to each fibre family (26).

$$\rho\phi_c = v_M \rho_M \phi_M + \sum_{i=1}^{N_{fam}} v_F^i \rho_F^i \phi_F^i \tag{26}$$

where ρ, ρ_M and ρ_F^i are the density of the composite material, the matrix material and the fibre family i, respectively. ϕ_M and ϕ_F^i are the state potentials of the matrix and the fibre family i, respectively. The state potential of the composite material has to verify Clausius–Duhem inequality, simplified here for isothermal transformations:

$$\sigma_c : D - \left[v_M \rho_M \frac{d\phi_M}{dt} + \sum_{i=1}^{N_{fam}} v_F^i \rho_F^i \frac{d\phi_F^i}{dt}\right] \geqslant 0 \tag{27}$$

where σ_c is the composite stress tensor. D is the rate of deformation tensor, assimilated to $\dot{\varepsilon}$ under the hypothesis of small perturbations. It is important to note that the composite strain tensor, ε, is here identical to the matrix strain tensor. In the framework of viscoelas ticity-viscoplasticity and small perturbations, the matrix state

potential, ϕ_M, is a function of $\varepsilon, \varepsilon^{ve}, \varepsilon^{vp}$ and κ, with notations of Section 2.1. If considering the strain partition $\varepsilon = \varepsilon^{ve} + \varepsilon^{vp}$, only three of these internal variables are actually independent. The time derivative of ϕ_M can therefore be expressed using the following partial derivatives form:

$$\frac{d\phi_M}{dt} = \frac{\partial \phi_M}{\partial \varepsilon} : \frac{\partial \varepsilon}{\partial t} + \frac{\partial \phi_M}{\partial \varepsilon^{vp}} : \frac{\partial \varepsilon^{vp}}{\partial t} + \frac{\partial \phi_M}{\partial \kappa} \cdot \frac{\partial \kappa}{\partial t} \tag{28}$$

Concerning the fibre media, each potential, ϕ_F^i, is a function of the scalar axial strain, $\varepsilon_F^{0,i}$ (23). Yet for convenience, the fibre Hencky strain tensors expressed in the global coordinate system by $\varepsilon_{F\,kl}^i = T_{k1}^i T_{1l}^{i^{-1}} \varepsilon_F^{0,i}, \forall k,l,\forall i$, are considered, so that $\frac{d\phi_F^i}{dt} = \frac{\partial \phi_F^i}{\partial \varepsilon_F^i} : \frac{\partial \varepsilon_F^i}{\partial t}, \forall i$. If assuming small displacements, the Hencky strain tensors can be assimilated to the Green–Lagrange strain tensors, $\mathscr{E}_F^i$. These ones are expressed from the right Cauchy-Green tensors by $\mathscr{E}_F^i = \frac{1}{2}\left(C_F^i - I\right), \forall i$. Relation (22) therefore leads to the approximation $\frac{\partial \varepsilon_F^i}{\partial t} \approx A^i \frac{\partial \varepsilon}{\partial t} A^i, \forall i$. Finally, noting that $X : \left(A^i Y A^i\right) = \left(A^i X A^i\right) : Y$, for any matrices X and Y, by construction of matrices A^i, these developpements give rise to a factorized expression of Clausius–Duhem inequality, given by Eq. (29).

$$\left[\sigma_c - v_M \rho_M \frac{\partial \phi_M}{\partial \varepsilon} - \sum_{i=1}^{N_{fam}} v_F^i \rho_F^i A^i \frac{\partial \phi_F^i}{\partial \varepsilon_F^i} A^i\right] : \dot{\varepsilon} - v_M \rho_M \left[\frac{\partial \phi_M}{\partial \varepsilon^{vp}} : \left(\frac{\partial \varepsilon^{vp}}{\partial t} - \frac{\partial \varepsilon^{ve}}{\partial t}\right) + \frac{\partial \phi_M}{\partial \kappa} \frac{\partial \kappa}{\partial t}\right] \geqslant 0 \tag{29}$$

The Clausius–Duhem inequality (29) has to be verified for any value of strain rate tensor, $\dot{\varepsilon}$. Then, considering the state laws $\rho_M \frac{\partial \phi_M}{\partial \varepsilon} = \sigma_M$ and $\rho_F^i \frac{\partial \phi_F^i}{\partial \varepsilon_F^i} = \sigma_F^i, \forall i$, the 3D stress state of the composite material expressed by Eq. (30) is an admissible solution.

$$\sigma_c = v_M \sigma_M + \sum_{i=1}^{N_{fam}} v_F^i A^i \sigma_F^i A^i \tag{30}$$

To validate the present modelling, numerically computed response of a polypropylene (PP) reinforced by 30 wt.% short glass fibres is compared to experimental results, for a wide range of loading directions and strain rates. Thus, a first step is to characterise the VE-VP behaviour of PP matrix based on Dynamic Mechanical Analysis and monotonic tensile and compression tests, as described in the following section.

3. Characterisation and validation of matrix behaviour model

The matrix material under investigation is a Polypropylene (PP) homopolymer (commercial grade Moplen HP500N by Lyon dell Basell) for injection moulding applications, with a MFR of 12 g · (10 min)$^{-1}$ and a density of 0.9 g · (cm)$^{-3}$. PP plates (200 mm-edge squares with a thickness of about 2.5 mm) are injection moulded following the process conditions prescribed by the supplier. In order to characterise the overall behaviour of PP matrix material, Dynamic Mechanical Analysis (DMA) and monotonic tensile and compression tests (at various loading speeds) are performed.

3.1. Dynamic Mechanical Analysis for the identification of parameters

For the determination of the viscoelastic parameters of PP matrix, small amplitude oscillatory tensile experiments are performed on an electromagnetic jack (INSTRON E3000) with a 3 kN cell force. The experiments are performed at room temperature. For these tests, flat rectangular specimens (50x10 mm^2, with a thickness of 2.5 mm) are cut in an injected plate. A sinusoidal strain (Eq. (31)), characterised by an angular frequency, ω, is applied to the specimen. Frequency is progressively increased from 0.01 H_z to 30 H_z with several loading cycles per frequency (Fig. 1 and Table 1) and 5 specimens are tested for each frequency.

$$\varepsilon(t) = \varepsilon_0 cos(\omega t) = \varepsilon_0 R_e\{exp(i\omega t)\} \tag{31}$$

ε_0 is the strain amplitude, t the time and R_e stands for the real part of any complex number. In the framework of small deformations, the stress response is sinusoidal as well, with the same pulsation, ω, but with a different amplitude, σ_0, and an out-of-phase angle (loss angle), δ, such that:

$$\sigma(t) = \sigma_0 cos(\omega t + \delta) = \sigma_0 R_e\{exp(i(\omega t + \delta(\omega)))\} \tag{32}$$

The complex modulus, E^*, is defined by the ratio of stress and strain as follows:

$$E^*(i\omega) = \frac{\sigma_0}{\varepsilon_0} exp(i\delta(\omega)) \tag{33}$$

E^* can be split into a real part, E', called storage modulus (associated to the elastic response) and an imaginary part, E'', called loss modulus (associated to the viscous response), so that $E^* = E' + iE''$, with $E' = \frac{\sigma_0}{\varepsilon_0} cos(\delta)$ and $E'' = \frac{\sigma_0}{\varepsilon_0} sin(\delta)$.

The Maxwell parameters are identified based on results of DMA. A 1D form of the hereditary integral expression of the stress–strain relation, Eq. (2), is expressed as follows:

$$\sigma(t) = \int_{-\infty}^{t} E(t-\zeta) \frac{d\varepsilon(\zeta)}{d\zeta} d\zeta \tag{34}$$

where $E(t)$ is the relaxation modulus. Considering that a finite number N of separate Maxwell elements are arranged in parallel with an elastic Hooke element (as presented in Section 2.1), $E(t)$ is expressed as follows:

$$E(t) = E_\infty + \sum_{i=1}^{N} E_i exp\left(-\frac{1}{\tau_i}\right) \tag{35}$$

E_i and τ_i correspond to the rigidity and relaxation time of the ith Maxwell element, respectively. E_∞ represents the long term modulus of the material. By substituting the deformation sinusoidal form, (Eq. (31)), into the hereditary integral expression (Eq. (34)), the complex modulus can be expressed as follows:

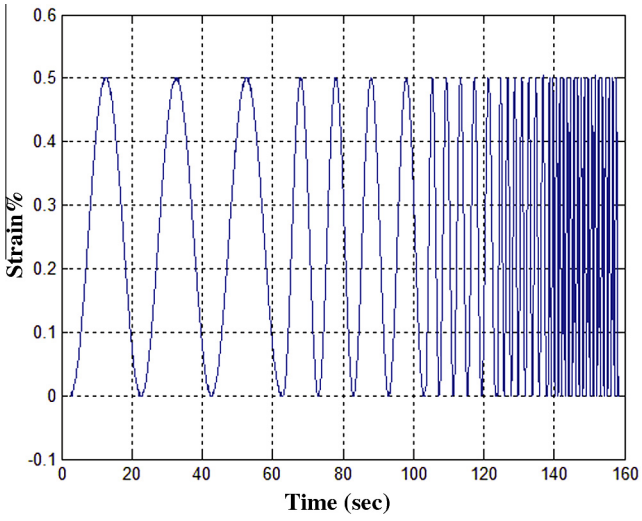

Fig. 1. An example of applied sinusoidal strain for frequencies equal to 0.05, 0.1, 0.25, 0.5 and 1 Hz.

Table 1
DMA cycles.

Frequencies (Hz)	Number of cycles
0.01	3
0.05	4
0.1	5
0.25	6
0.5	8
1	21
10	201
20	301
30	301

$$E^*(i\omega) = i\omega \int_0^\infty E(t)exp(-i\omega t)dt \tag{36}$$

By expressing the time dependent modulus, $E(t)$, in its Prony series form (Eq. (35)), the complex modulus can be expressed as follows:

$$E^* = E_\infty + \sum_{i=1}^{N} E_i \frac{(\omega\tau_i)^2}{1+(\omega\tau_i)^2} + i\sum_{i=1}^{N} E_i \frac{\omega\tau_i}{1+(\omega\tau_i)^2} \tag{37}$$

The storage and loss moduli are therefore expressed by:

$$E' = E_\infty + \sum_{i=1}^{N} E_i \frac{(\omega\tau_i)^2}{1+(\omega\tau_i)^2} \tag{38a}$$

$$E'' = \sum_{i=1}^{N} E_i \frac{\omega\tau_i}{1+(\omega\tau_i)^2} \tag{38b}$$

The parameters E_i and τ_i are found following a least square minimization algorithm (Eq. (39)).

$$_{E_i,\tau_i} min \sum_{i=1}^{M} \left[\left(\frac{E'(\omega_j)}{E'_{exp}(\omega_j)} - 1 \right)^2 + \left(\frac{E''(\omega_j)}{E''_{exp}(\omega_j)} - 1 \right)^2 \right] \tag{39}$$

where E'_{exp} and E''_{exp} are obtained from measured data at pulsation $\omega_j, j \in \{1,\ldots,M\}$, with M the number of imposed frequencies. The identified viscoelastic parameters for a model composed of 7 Maxwel elements are listed in Table 2. Comparisons between the computed (from the Maxwell generalised model (Eq. (38b))) and measured moduli are presented in Fig. 2.

3.2. Monotonic tests for the identification of viscoplastic parameters

For the characterisation of the viscoplastic behaviour of unreinforced PP matrix, quasi-static and dynamic monotonic tensile tests are performed. Specimens are cut by water jet in the injection-moulded plates and tested at room temperature.

Quasi-static tensile tests are carried out using Instron E3000 electromagnetic jack (3 kN cell force). The specimen geometry follows ISO527 norm (Fig. 3a). Displacement rates of 1, 10 and 60 mm · min^{-1} are imposed, corresponding respectively to strain rates of 5.55 · 10^{-4} s^{-1}, 5.55 · 10^{-3} s^{-1} and 3.33 · 10^{-2} s^{-1} (for a region of interest (ROI) of 30 mm height). Dynamic tensile tests are carried out using Instron 65/20 hydraulic jack. A piezoelectric load cell was fixed on the rigid frame of the jack. A specific set-up for dynamic test, developped in LAMIH to prevent specimen loading as long as imposed test velocity is not reached, is used to clamp the specimen. The specimen geometry is specially designed to this set-up (Fig. 3b). The imposed displacement rates are of 10, 100 and 1000 mm · s^{-1}, corresponding to strain rates of 0.5 s^{-1}, 5 s^{-1} and 50 s^{-1}, respectively (for a 20-mm-heigth ROI). For both quasi-static and dynamic tensile tests, nominal axial stress, σ, is computed as the ratio of load, F, measured by the cell force, by initial cross-section at the centre of the ROI, S_0, i.e. $\sigma = F/S_0$.

True displacement and true in-plane strain fields are determined using Digital Image Correlation (DIC) technique [40]. A black and white random pattern is created on specimen surface. As

Table 2
Identified linear viscoelastic parameters of the PP matrix material.

Coefficients E_i (MPa)	Relaxation times τ_i (s)
495.78	10^{+3}
267.51	10^{+2}
249.68	10
195.66	1
151.59	10^{-1}
94.06	10^{-2}
59.12	10^{-3}
E_∞ (MPa)	486.93

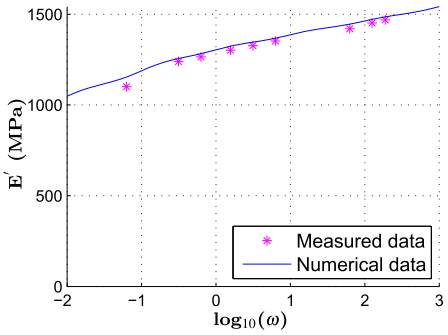

(a) Storage modulus versus logarithmic form of angular pulsation

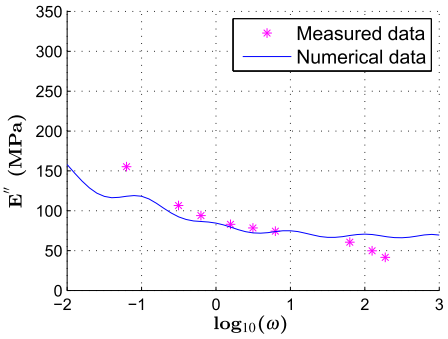

(b) Loss modulus versus logarithmic form of angular pulsation

Fig. 2. Comparison of measured and computed loss and storage moduli.

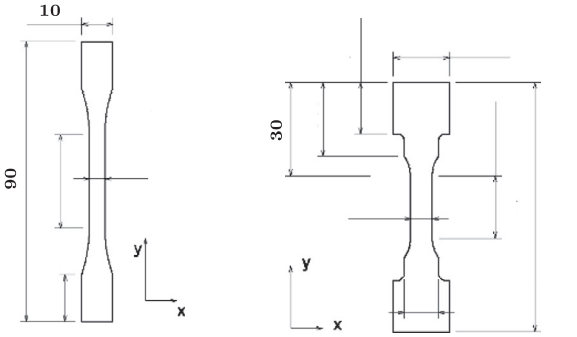

(a) Quasi-static tests specimen (b) Dynamic tests specimen

Fig. 3. Geometry of tensile specimens.

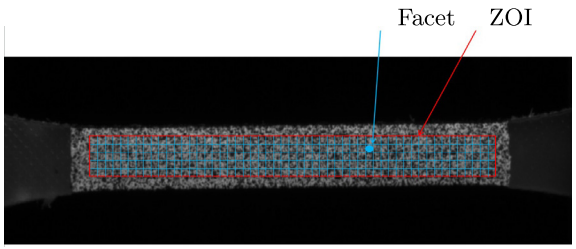

Fig. 4. Definition of the facets and the ROI for the strain field measurement.

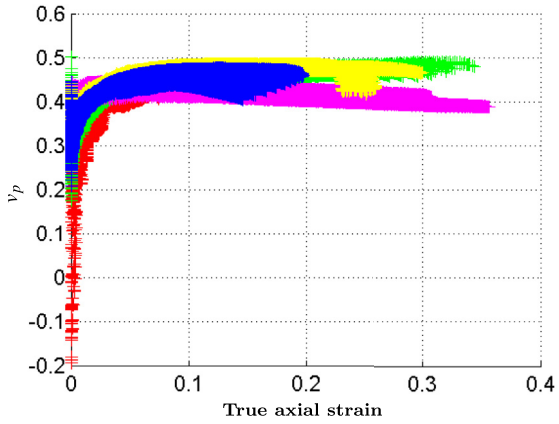

Fig. 5. Evolution of the viscoplastic Poisson ratio versus true axial strain.

shown in Fig. 4, the pattern is divided into sub-pixel zones (facets or zone of interest (ZOI)), each of them being characterised by a unique signature in grey level. The facets are tracked by DIC software (VIC 2D) so that in-plane displacement of facet centres are determined with respect to a reference image (recorded at an undeformed stage). In-plane strains at the centre of each facet are then computed. A facet size of 21×21 pix^2 is selected as the one leading to the best compromise between noise and spatial resolution, based on tests of rigid body motion.

To complete the characterisation of matrix behaviour, uni-axial compression tests are carried out on electromagnetic device INSTRON E3000 at a crosshead speed of 0.08 mm $\cdot$ min^{-1}. Specimens are cylinders (diameter of 5 mm) cut by water jet in the injected plates, so that their height is about 2.5 mm. The corresponding equivalent strain rate is then of $5 \cdot 10^{-4}$ s^{-1}. It is to note that five specimens are tested for every loading speed test. These monotonic tests are exploited to identify the PP matrix viscoplastic parameters, as described below.

Parameters a^+ and a^- (Eq. (14)) define the expansion and compaction of the viscoplastic flow associated to tension and compression, respectively, as presented in Section 2.1. The expansion can be characterised, in the case of tensile tests, from the (visco) plastic Poisson coefficient, ν_p, which is the ratio between the transversal, ε_{xx}^{vp}, and axial, ε_{yy}^{vp}, viscoplastic strain components ($\nu_p = -\varepsilon_{xx}^{vp}/\varepsilon_{yy}^{vp}$). ν_p is calculated using data obtained over all the ZOI and all the loading speeds (i.e., quasi-static and dynamic) by neglecting the elastic part of the total strain (i.e. $\varepsilon_{ij}^{vp} \simeq \varepsilon_{ij} \quad \forall ij$). Fig. 5 shows the evolution of the (visco) plastic Poisson ratio in function of true axial strain for all the loading speeds and for all the ZOI. It can be seen that the evolution is scattered for the very low strain values and tends to be constant for higher ones (when ε^{ve} acrually becomes neglectible compared to ε^{vp}). The (visco) plastic Poisson ratio is therefore identified for strain level higher than 0.02. As for this strain values ν_p is rather constant, it can be expressed in terms of incremental VP strain components, i.e. $\nu_p \simeq -\triangle\varepsilon_{xx}^{vp}/\triangle\varepsilon_{yy}^{vp}$. Considering the incremental form of the VP strain tensor under tensile loading (i.e. $\langle -I_1 \rangle = 0$ (Eq. (40)) the expression of ν_p is given by Eq. (41).

$$\Delta\varepsilon^{vp} = \Delta\lambda \frac{\frac{3}{2}S_M + \frac{1}{9}(a^+\langle I_1\rangle + a^-\langle -I_1\rangle)I}{\sqrt{3I_2 + \frac{1}{27}\left(a^+\langle I_1\rangle^2 + a^-\langle -I_1\rangle^2\right)}} \tag{40}$$

$$\nu_p = -\frac{\frac{3}{2}S_{xx} + \frac{1}{9}a^+I_1}{\frac{3}{2}S_{yy} + \frac{1}{9}a^+I_1} \tag{41}$$

Reminding the definition of the deviatoric stress tensor, **S**, Eq. (41) becomes:

$$\nu_p = -\frac{\frac{3}{2}\left(-\frac{1}{3}I_1\right) + \frac{1}{9}a^+I_1}{\frac{3}{2}\left(\sigma_{yy} - \frac{1}{3}I_1\right) + \frac{1}{9}a^+I_1} \tag{42}$$

The expression of the expansion parameter a^+ is finally given by:

$$a^+ = \frac{9}{2}\left(\frac{1-2\nu_p}{1+\nu_p}\right) \tag{43}$$

With an identified value of ν_p equal to 0.43, the expansion parameter a^+ is equal to 0.44. A similar analysis should be done under uniaxial compression loading in order to identify the compaction parameter a^-. Unfortunately the small size of the compression specimen did not allow the use of Digital Image Correlation technique and only axial displacements were measured by optical extensometry. Therefore incompressibility will be assumed in the

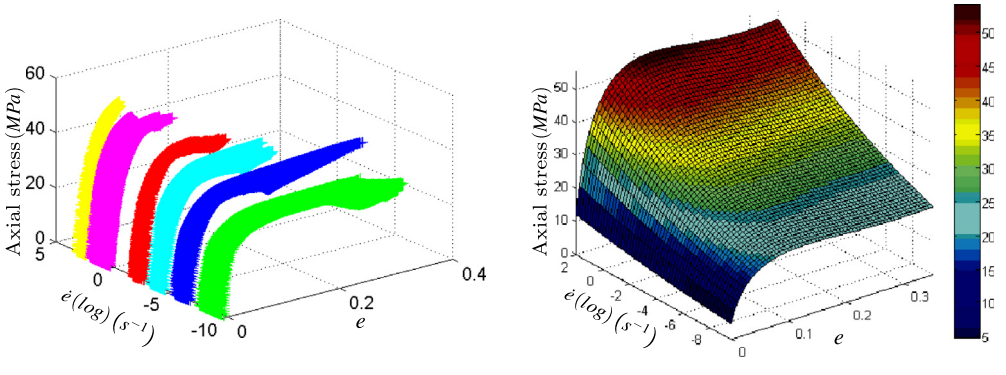

(a) True behaviour laws (b) Correlated behaviour surface

Fig. 6. Behaviour laws obtained with the *SEE*̇ method.

case of compression loading and a^- has the value of zero in the following. It is worth noting that it will not biased the validation of the SFRC behaviour modelling as long as only tensile loadings are considered. The use of Digital Image Correlation technique allows the determination of local displacements (i.e. on each ZOI) and therefore local strain and local strain rate throughout the test. Then, using the assumption of transverse isotropy, the true tensile stress of each ZOI is calculated as follows:

Table 3
Constitutive parameters.

Parameters	Value
σ_t (11)	7 MPa
h_1 (12)	35.40 MPa
h_2 (12)	2.17
h_3 (12)	58.78
$\dot{\kappa_0}$ (18)	10^{-5} s^{-1}
m (18)	0.02
a^+ 14)	0.61
a^- (14)	0
η (11)	2.04

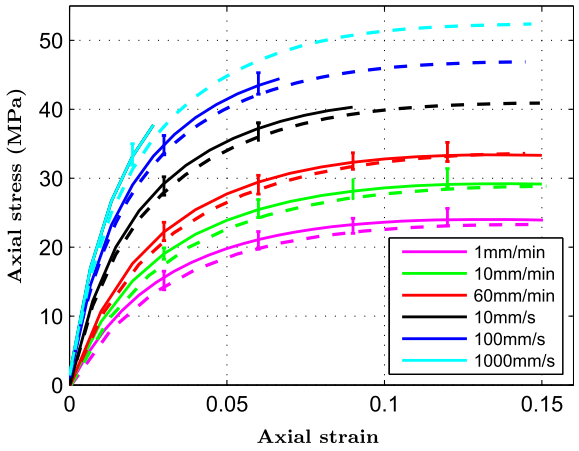

Fig. 7. Comparison between modelled and experimental tensile behaviour of PP at different loading rates (Continuous lines = Experimental data, Dashed lines = Numerical data) with vertical bars delimited by minimum and maximum values.

$$\sigma_{yy_i} = \frac{F}{S_0} exp(-2\varepsilon_{xx_i}) \tag{44}$$

where ε_{xx_i} is the true transversal strain of the ith ZOI. According to the $SE\dot{E}$ method, developped by Lauro et al. [11], points of coordinates $(\sigma_{yy_i}, e_i, \dot{e}_i)$ are plotted in the stress, strain and strain rate space to form the $SE\dot{E}$ ("Stress, Epsilon, Epsilon dot") surface. e_i is the equivalent true strain expressed as follows:

$$e_i = \int_t \sqrt{\frac{2}{3}\dot{\varepsilon} : \dot{\varepsilon}} dt \tag{45}$$

This surface represents material's behaviour for a large strain rate range (Fig. 6a). The hardening and viscoplasticity parameters $(h_1, h_2, h_3, m$ and $\dot{\kappa_0})$ are determined by fitting the overstress expression (Eqs. (12) and (18)) with the behaviour surface (Fig. 6b). Note that the equivalent strain and equivalent strain rate are assumed here to be equal to the equivalent viscoplastic strain, κ, and equivalent viscoplastic strain rate, $\dot{\kappa}$, respectively.

It is to note that in the constitutive model the yield stress, σ_t, is identified here as the stress from which the true stress–strain curve becomes non-linear (7 MPa). This leads to a true equivalent viscoplastic threshold of about 0.5% which justifies the later assumption. Finally, the pressure dependency parameter η (Eq. (11)), is defined as the ratio of the compression and tension initial yield stresses, is identified. To do that, tensile and compression yield stresses must be measured for tests realized at identical

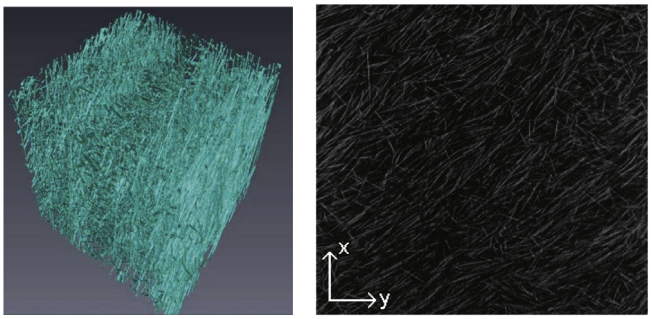

(a) 3D recontruction (b) 2D slice from scanned volume

Fig. 9. Reconstructed microstructure of PP-30GF by micro-computed tomography.

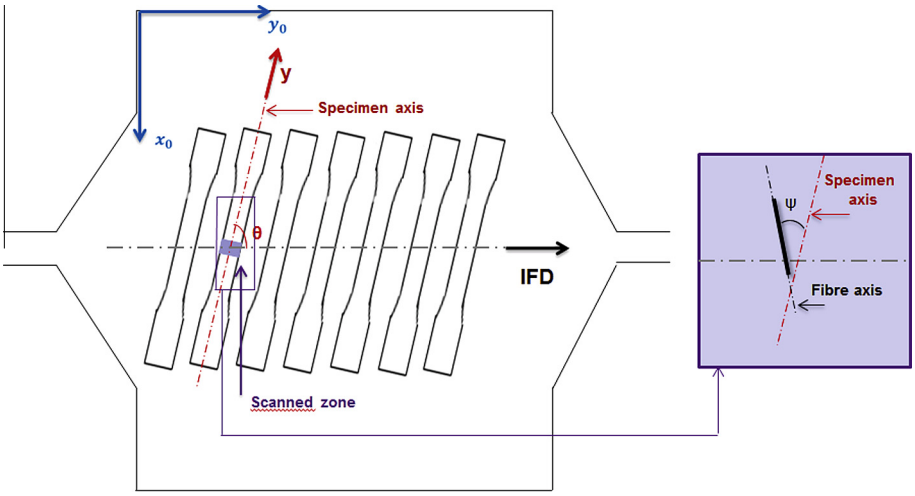

Fig. 8. Definition of angles θ and ψ.

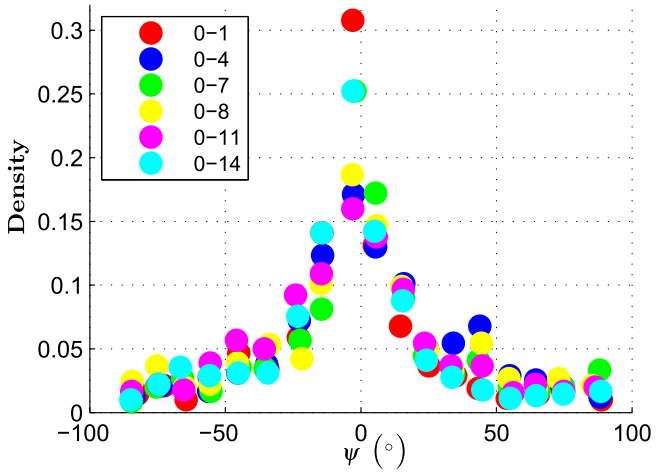

(a) Distribution of fibre orientation at $\theta = 0^\circ$

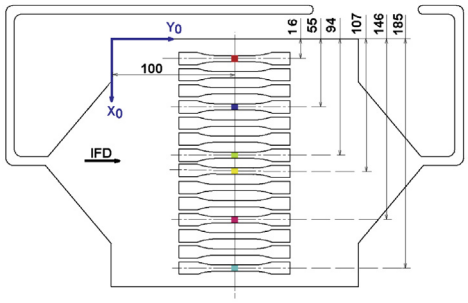

(b) Injection moulded plate with 0°-specimens cut at different locations

Fig. 10. Distribution of fibre orientation in scanned volume of specimens cut at different plate locations and 0° with respect to IFD.

strain rates. The uniaxial tensile and compression tests corresponding to a strain rate of $5.55 \cdot 10^{-4}\ s^{-1}$ (realised respectively at 1 mm/min and 0.08 mm/min) are therefore considered. With determined tensile and yield stresses of 29 MPa and 14 MPa, respectively, a value of 2.071 is obtained for η.

Parameters involved in the matrix constitutive model are listed in Table 3.

3.3. Evaluation of the matrix constitutive model

The relevance of the implemented constitutive model for the matrix material is assessed through its capacity to reproduce the experimental response of PP material over a relatively large range of strain rates. To this end, the constitutive equations presented in Section 2 are implemented in Abaqus 6.11 subroutine VUMAT (explicit temporal integration scheme). Uniaxial tensile tests of PP matrix are then simulated, using the parameters identified in Section 3 (Table 3). Obviously, fibre volume fraction is null in the present numerical tests. Tensile tests are simulated at the same quasi-static (1, 10 and 60 mm/min) and dynamic (10, 100 and 1000 mm/s) loading speeds as during experiments. 8 nodes, full integration elements (C3D8) are used. All degrees of freedom are locked at the basis of the specimen and the loading consists on a prescribed monotonic velocity on nodes of the upper edge. Numerical results are compared with experimental data (averaged over the five tests realised for each loading speed) in Fig. 7. In this figure, numerical and experimental data are averaged upon all the ROI (height of 15 and 20 mm in quasi-static and dynamic tests, respectively). In fact, strain fields obtained both numerically and from DIC measurements were verified to be homogeneous enough in the ROI so that the comparison of averaged strains is reliable for the validation of the model. Finally, results show that the numeri-

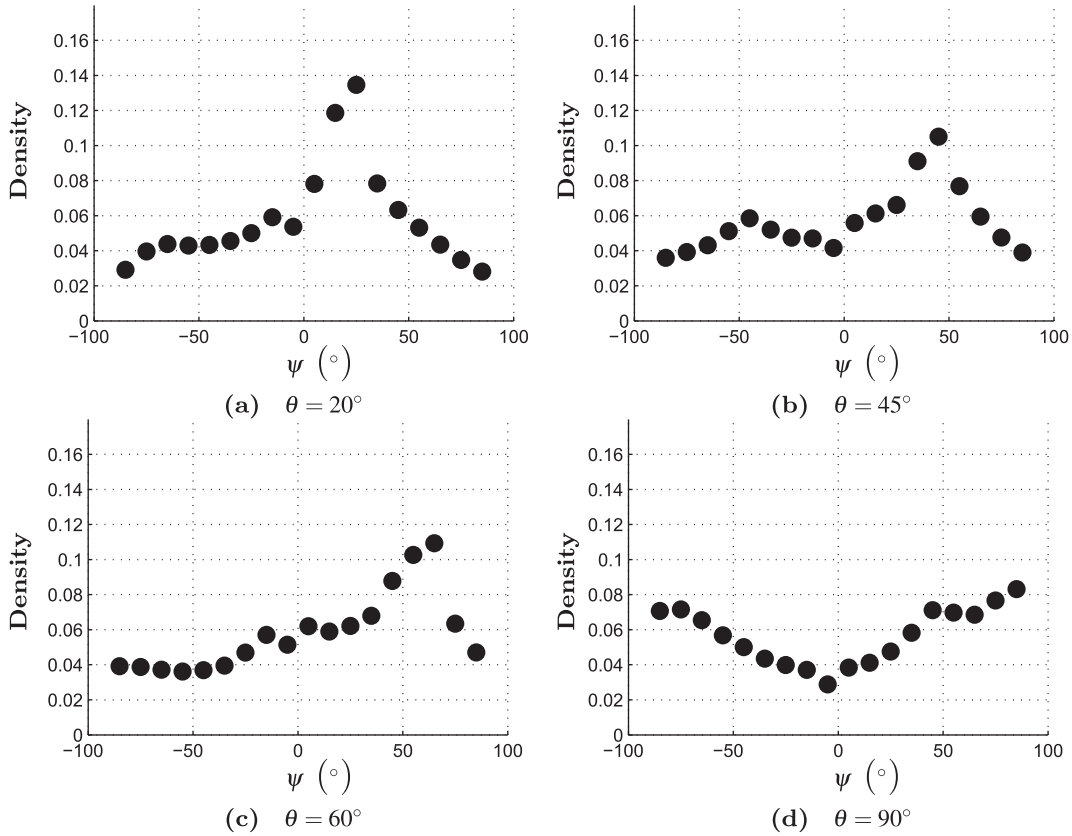

(a) $\theta = 20^\circ$ (b) $\theta = 45^\circ$ (c) $\theta = 60^\circ$ (d) $\theta = 90^\circ$

Fig. 11. Distribution of fibre orientation in scanned volume of specimens cut at angles equal to 20°, 45°, 60° and 90° with respect to IFD.

cal model is in agreement with experimental data at all investigated loading rates.

4. Characterisation and validation of SFRC behaviour model

The composite material under investigation (hereafter called PP-30GF) is commercial grade ALTECH PP-H A 2030/159 GF30 CP, supplied by Albis, and obtained by reinforcing a homopolymer polypropylene (PP) matrix with 30 wt.% of short-glass fibres with chemical coupling. PP-30GF has a MFR of 2 g.$(10\ \text{min})^{-1}$ and a density of 1.12 g $\cdot$ cm^{-3}. PP-30GF plates (200 mm-edge-squares with a thickness of about 2.5 mm) are injection moulded following the process conditions prescribed by the supplier. Quasi-static and dynamic PP-30GF specimens, with geometries identical to the PP ones (Fig. 3), are cut at different angles, θ, with respect to the injection flow direction (IFD) ($\theta = 0^\circ, 20^\circ, 45^\circ, 60^\circ$ and 90°, Fig. 8). In this Section, the microstructure of the SFRC is investigated in the central volume of some selected specimens using micro computed tomography, aiming at the characterisation of fibres' orientation. In accordance to the "families of fibres" concept presented in Section 2.2, fibres are afterwards divided into a finite number of families. Volume fractions attributed to fibre families are those corresponding to real distribution of orientation obtained by micro-computed tomography.

4.1. Characterisation of composite micro-structure by micro-computed tomography

The distribution of fibre orientation in the injected plates of PP-30GF is investigated by X-ray micro-computed tomography (μ-CT) using high-resolution microtomograph Skyscan 1172 (Bruker Micro CT). A rotation step of 0.4°, voltage of 30 kV and current of 40 µA are used, leading to a spatial resolution (voxel size) of 3.87 µm. Some quasi-static specimens (ISO527-type), cut at different angles θ with respect to the injection flow direction (IFD) ($\theta = 0^\circ, 20^\circ, 45^\circ, 60^\circ$ and 90°), are selected for micro-tomography analysis. A volume centred on the specimen region of interest (ROI), with a height of about 5 mm and covering all specimen width and thickness, is scanned (Fig. 8). A 3D representation of the PP-30GF microstructure is obtained using data acquired by μ-CT (Fig. 9a). Reconstructed 3D microstructures show that the vast majority of fibres present a very low out-of-plane angle (i.e. with respect to the (x, y) plane, with y the specimen axis and z oriented along thickness). In all the following, fibres are therefore assumed to have in-plane orientation. Sets of 2D greyscale images, in the (x, y) plane, are extracted from slices of the 3D view, at regular spaced positions in thickness direction (Fig. 9b). Fibres are first isolated from matrix material, using Fiji tools of Image J software [41], by applying a grey-level thresholding to the images (based on Otsu mehtod). Fiji tools of structure detection and analysis were applied to 2D images in order to identify and count fibres and determine their characteristics (length, diameter and orientation).

In order to obtain orientation histograms, density of fibres characterised by an angle ψ with respect to specimen axis within the intervals $[\alpha; \alpha + 10^\circ[$, for α varying from -90° to 80°, are determined.

Histograms for scanned θ-specimens (i.e. characterised by a cutting angle θ) are presented in Figs. 10 and 11. First, it can be seen that fibre orientations in 0°-specimens are distributed around the value 0° as a preferential orientation (Fig. 10). More generally, preferential orientation of fibres is IFD, i.e. equal to $\pm\theta$ with respect to the specimen axis for all values of θ, as expected (Fig. 11). Histograms obtained for 0°-specimens show that fibres distribution of orientation depends on specimen location in the plate. For instance, as illustrated by specimen 0–1, the distribution curve tends to be sharper around IFD direction near plate edge (i.e. fraction of fibres that are oriented in IFD increases). In addition, it is worth noting that fibre orientation evolves in the thickness direction in accordance with the well-known skin-shell-core phenomenon [42]. In fact, angle of fibre orientation tends to increase in plate skins, where fibres tend to orient randomly, then decreases in shell layers, where fibres are preferentially oriented along IFD,

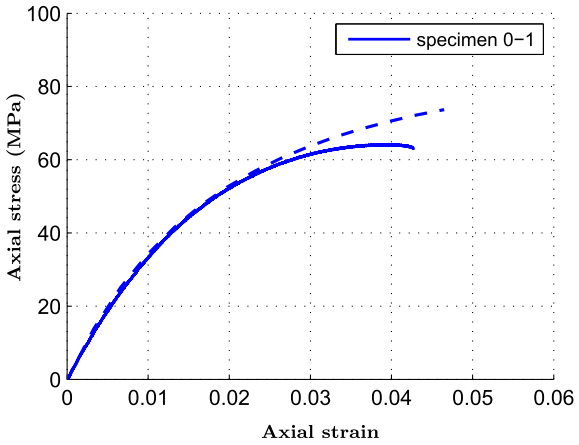

Fig. 12. Identification of the IFSS (Continuous line = Experimental data, Dashed line = Numerical data).

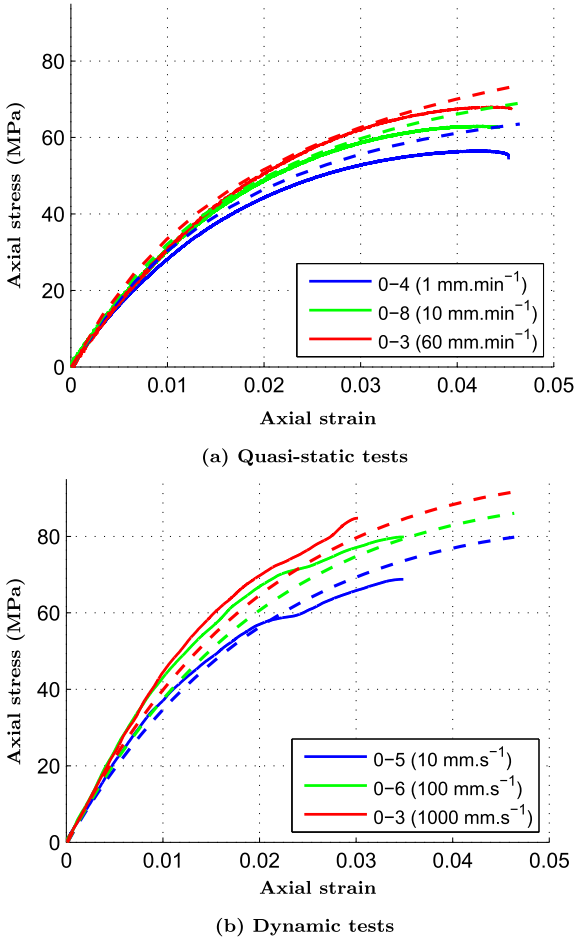

Fig. 13. Comparison of experimental and numerical data for tests of 0° specimens (Continuous lines = Experimental data, Dashed lines = Numerical data).

and increases again in core layer where fibres tend to orient transversally to IFD. This layered structure results from the combination of shear flow and fountain flow in injection moulded process [43].

As the microstructure of the selected specimens is characterised, actual distribution of orientation will be taken into consideration as input data in the evaluation of the implemented SFRC behaviour model.

4.2. Tensile tests

In order to characterise the behaviour of the composite material (PP30GF) and validate the implementation of the composite behaviour model, quasi-static and dynamic tensile tests are performed at various loading speeds and for all values of cutting angle θ. Same testing devices and specimen geometries as for PP are used, as well as same imposed quasi-static and dynamic displacement rates. As tensile behaviour of the composite material is expected to be more brittle than that of unreinforced PP and therefore limited to low strain levels, DIC technique is not used for PP-30GF. Instead, axial displacements are measured by optical extensometry, i.e. non-contact elongation measurement based on motion tracking of black-and-white transition lines. For quasi-static tests, optical extensometer ZS16D (CCD line scan sensor – Rudolf GmbH), with a precision of 3 µm over 50 mm, is used. Elongation of a black-painted area of 15 mm height, centred in the ROI, is followed. Axial strain is computed as the ratio of measured axial elongation by the initial length of 15 mm. For dynamic tests, optical extensometer 200XR (Rudolf GmbH – precision of 5 µm over 50 mm), which allows higher acquisition frequency, is used with a tracked zone covering all specimen's ROI (i.e. gauge length of 20 mm).

4.3. Validation of the composite constitutive model

As described in Section 4.1, the composite material is characterised by a distribution of fibre orientation having the injection flow direction (IFD) as preferential orientation. In the modelling, 10 families of fibres are considered with angles of orientation, α, varying from 0° to 90° by step of 10°. Corresponding volume fractions are computed consistently with the identified distributions. The tensile tests realised for PP-30GF specimens with different cutting angles and at different loading rates (Section 4.2) are simulated taking into account actual fibre orientations. In fact, all PP-30GF specimens were not analysed by μ-CT. Then, distributions of fibre orientation in specimens that were not scanned are assumed to be identical to that of scanned specimens located at approximately the same position in the plate. The same geometries and boundary conditions are used as in the case of simulation of PP specimens (Section 3.3). As presented in Section 2.2, fibres have a linear elastic behaviour. All fibres are assumed to have the same young modulus, E_F, equal to 76 GPa. Length, L, and radius, r, are respectively equal to 0.24 mm and 5 µm. The last parameter to be introduced for the fibre stress computation is the interfacial shear strength (IFSS), τ. In fact, this parameter depends in particular on the nature of the matrix and fibres, process conditions and fibre volume fraction [44–46]. The experimental identification of

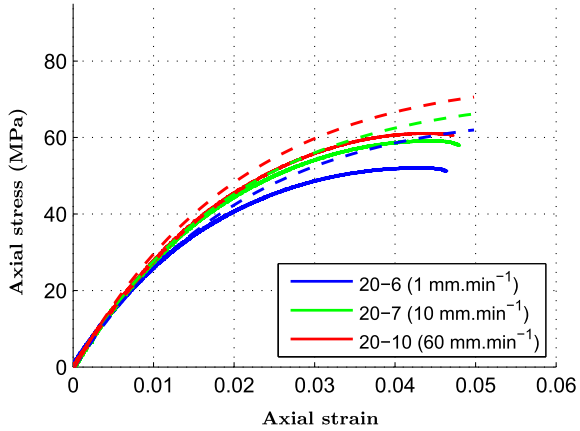

(a) Quasi-static tests

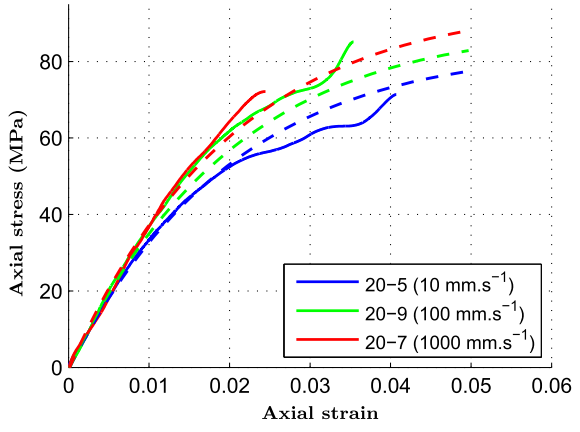

(b) Dynamic tests

Fig. 14. Comparison of experimental and numerical data for tests of 20° specimens (Continuous lines = Experimental data, Dashed lines = Numerical data).

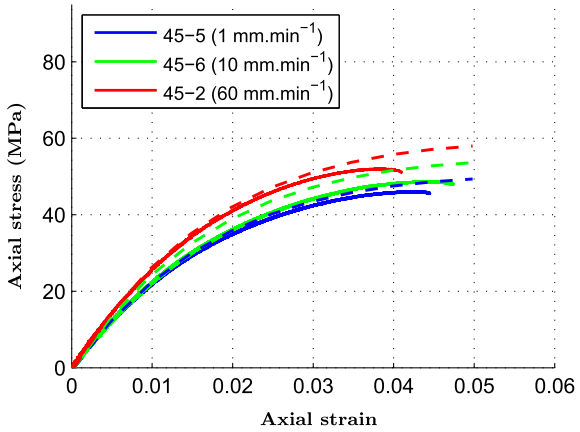

(a) Quasi-static tests

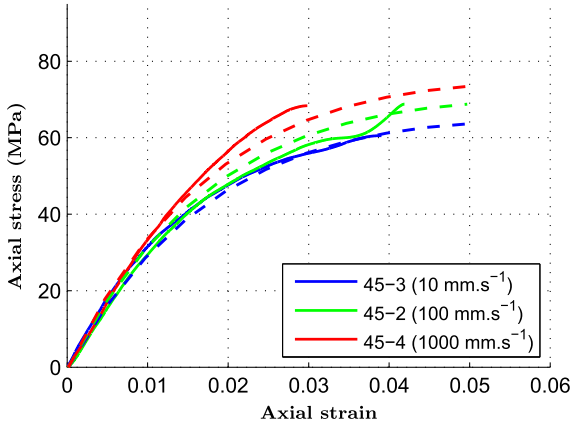

(b) Dynamic tests

Fig. 15. Comparison of experimental and numerical data for tests of 45° specimens (Continuous lines = Experimental data, Dashed lines = Numerical data).

the IFSS is not in the scope of this work. Therefore, it is determined as the one leading to the best fit with experimental results in the case of a PP-30GF specimen tested at 0° and at the lowest loading rate (i.e. 1 mm · min^{-1}). More precisely, the specimen 0–1 is considered, as the one presenting the highest fraction of fibres oriented in tensile direction (Fig. 10). Fig. 12 presents numerical results obtained with a value of $\tau = 23$ MPa leading to the best fit between experimental and numerical responses.

The relevance of the developped constitutive model is then evaluated using the set of identified parameters and distrubtion of fibre orientation. Experimental results obtained for tensile tests at quasi-static and dynamic loading rates are compared with numerical responses of the composite model for all cutting angles (0°, 20°, 45°, 60° and 90°). Results presented in Figs. 13–17 demonstrate the accuracy of the implemented model, since the stress–strain response is well reproduced for the different cases. A limitation was however noted as the tensile strain increases in the quasi-static case. Actually a softening in the stress–strain curves is observed on the experimental results and is not predicted by the current constitutive model. An explanation is that this phenomena is due to the developpement of damage mechanisms, mainly fibre–matrix decohesion, which are not taken into account in the present model. It is also observed that this softening is more important at lower loading angles with respect to IFD (0° and 20°), which reveals the possible anisotropy of these damage mechanisms. The characterisation and the modelling of the debonding mechanisms and their dependency on the strain rate are the object of ongoing work.

5. Conclusions

A strain-rate dependent behaviour model for SFRC is presented here, based on an original approach that aims to be an efficient alternative to more complex procedures of homogenisation. This work presents the extension of this approach to strain rate dependent composite behaviour (i.e. viscoelastic and/or viscoplastic). Complex fibre orientations, including distributed and random orientations can be modelled in a simple way. The implemented constitutive laws are first described in details, begining with coupled viscoelastic–viscoplastic scheme of matrix behaviour. Then constitutive equations of composite bahviour model are detailed. The accuracy of the modelling is assessed for the case of a PP reinforced by 30 wt.% of short-glass fibres by comparison of numerical results with experimental ones. To this end, constitutive parameters involved in the matrix behaviour law are identified based on dynamic mechanical analysis, compression and tensile tests under a wide range of strain rates. Then dealing with the case of injection-moulded PP-short glass fibre composite, a first step is to characterise the actual distribution of fibre orientation using micro-computed tomography. Orientations thus identified were input of the behaviour model according to the "families of fibres" concept. A comparison of numerical and experimental results obtained for PP material is performed in order to validate the implementation of the matrix behaviour model. Then simulated quasi-static and dynamic tensile tests of PP-GF composite proved the consistency of the implemented model.

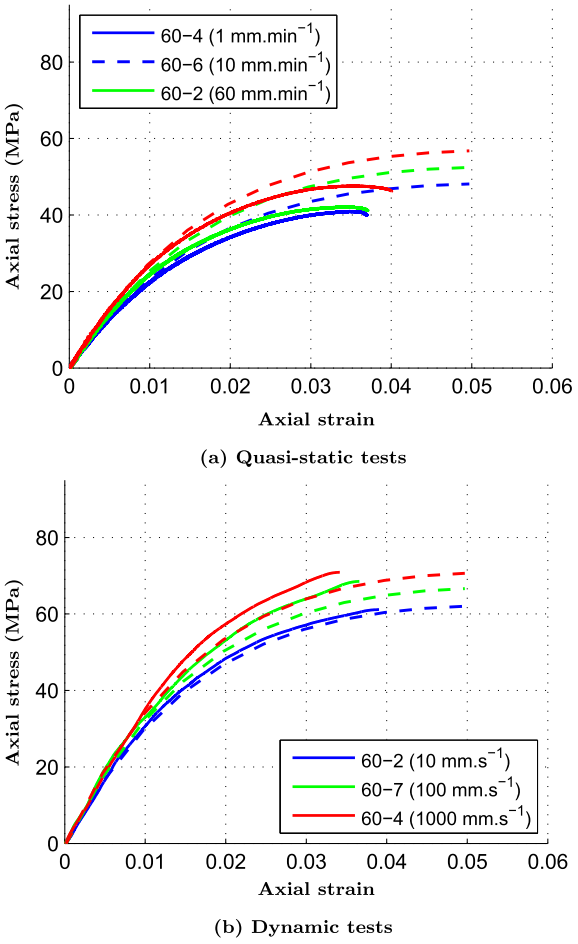

Fig. 16. Comparison of experimental and numerical data for tests of 60° specimens (Continuous lines = Experimental data, Dashed lines = Numerical data).

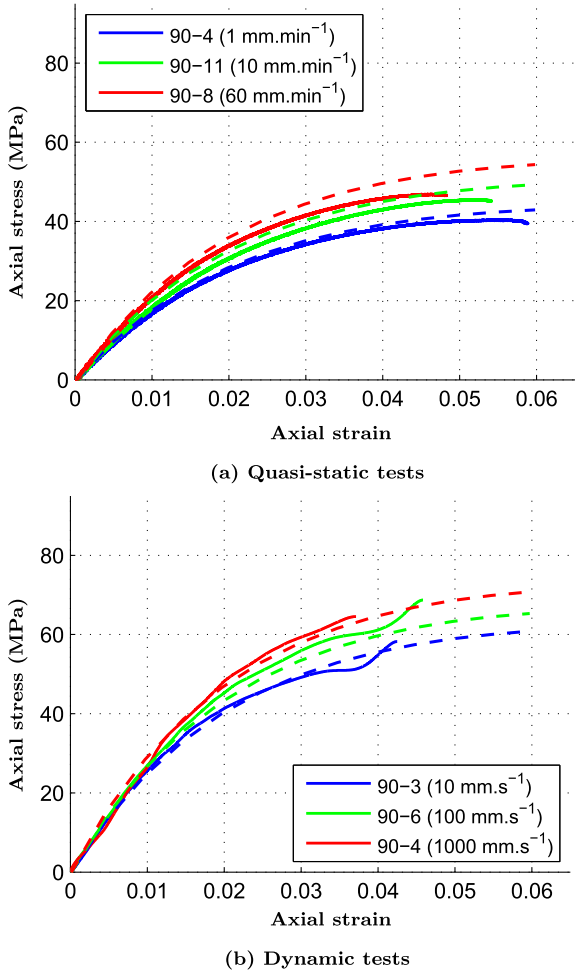

Fig. 17. Comparison of experimental and numerical data for tests of 90° specimens (Continuous lines = Experimental data, Dashed lines = Numerical data).

The advantageous adaptability of the present modelling offers the possibility to go further with the matrix material modelling. Hence, introducing non-linearities in the modelling of matrix viscoelasticity will be addressed in a future work, for instance in the case of composites with very low volume fraction of reinforcement. Moreover, experimental investigations are to be extended to the case of loading/unloading tests for the direct verification of the Kuhn-Tucker condition introduced in the current matrix model. Finally, further work concerns the introduction of damage mechanisms in the behaviour prediction by the implementation of a fibre-matrix debonding model.

Acknowledgements

This research is conducted through collaboration between the University of Valenciennes et du Hainaut-Cambrésis and the National Engineering School of Sfax. This collaboration is jointly financed in the frame of the Utique CMCU programme. The present research work has been supported by International Campus on Safety and Intermodality in Transportation, the Région Nord Pas de Calais, the European Community, the Délégation Régionale à la Recherche et à la Téchnologie, the Ministère de ÍEnseignement Supérieur et de la Recherche, and the Centre National de la Recherche Scientifique: the authors gratefully acknowledge the support of these institutions.

References

[1] Bernasconi A, Cosmi F, Dreossi D. Local anisotropy analysis of injection moulded fibre reinforced polymer composites. Compos Sci Technol 2008;68:2574–81.
[2] Vincent M, Devilliers E, Agassant JF. Fibre orientation calculation in injection moulding of reinforced thermoplastics. J Non-Newtonian Fluid Mech 1997;73:317–26.
[3] Parsons E, Boyce MC, Parks DM. An experimental investigation of the large-strain tensile behavior of neat and rubber-toughned polycarbonate. Polymer 2004;45:2665–84.
[4] Lai J, Bakker A. An integral constitutive equation for nonlinear plasto-viscoelastic behavior of high-density polyethylene. Polym Eng Sci 1995;35:17.
[5] Drozdov A. Creep rupture and viscoelastoplasticity of polypropylene. Eng Fract Mech 2010;77:2277–93.
[6] Drozdov A. Multi-cycle viscoplastic deformation of polypropylene. Comput Mater Sci 2011;50:1991–2000.
[7] Khan A, Zhang H. Finite deformation of a polymer: experiments and modeling. Int J Plast 2001;17:1167–88.
[8] Kajberg J, Sundin KG, Melin LG, Stahle P. High strain-rate tensile testing and viscoplastic parameter identification using microscopic high-speed photography. Int J Plast 2004;20:561–75.
[9] Notta-Cuvier D, Langrand B, Lauro F, Markiewicz E. An innovative procedure for characterising a coupled elastoplastic damage model of behaviour using the Virtual Fields Method. Int J Solids Struct 2015;69–70:415–27.
[10] Pierron F, Grediac M. The virtual fields method. Extracting constitutive mechanical parameters from full-field deformation measurements. Springer; 2012.
[11] Lauro F, Bennani B, Morin D, Epee AF. The SEÈ method for determination of behaviour laws for strain rate dependent material: application to polymer material. Int J Impact Eng 2010;37:715–22.
[12] Charles III LT, Liang E. Stiffness prediction for unidirectional short-fiber composites: review and evaluation. Compos Sci Technol 1999;59:655–71.
[13] Smit RJM, Brekelmans WAM, Meijer HEH. Prediction of the mechanical behavior of nonlinear heterogeneous systems by multi-level element modeling. Comput Methods Appl Mech Eng 1998;155:181–92.
[14] Ghosh S, LeeK K, Moorthy S. Two scale analysis of heterogeneous elastic-plastic materials with asymptotic homogenization and Voronoi cell finite element model. Comput Methods Appl Mech Eng 1996;132:63–116.
[15] Eshelby JD. The determination of the elastic field of an ellipsoid inclusion, and related problems. Proc R Soc London A 1997;241:376–96.
[16] Mori T, Tanaka K. Average stress in matrix and average elastic energy of materials with misfitting inclusions. Acta Metall 1973;21:571–4.
[17] Hershey AV. The elasticity of an siotropic aggregate of anisotropic cubic crystals. J Appl Mech 1954;21:236–40.
[18] Hill R. A self-consistent mechanics of composite materials. J Mech Phys Solids 1965;13:89–101.
[19] Nemat-Nasser S, Hori M. Micromechanics: overall properties of heterogeneous materials. second ed. Amsterdam: Elsevier; 1999.
[20] Berveiller M, Zaoui A. An extension of the self-consistent scheme to plastically-flowing polycrystals. J Mech Phys Solids 1979;26:325–44.
[21] Tandon GP, Weng GJ. A theory of particle-reinforced plasticity. J Appl Mech 1988;55:126–35.
[22] Molinari A. Averaging models for heterogeneous viscoplastic and elasto-viscoplastic materials. J Eng Mater Technol 2002;124:62–70.
[23] Masson R, Bornert M, Suquet P, Zaoui A. An affine formulation for the prediction of the effective properties of nonlinear composites and polycrystals. J Mech Phys Solids 2000;48:1203–27.
[24] Fiebel C, Doghri I, Legat V. General mean-field homogenization schemes for viscoelastic composites containing multiple phases of coated inclusions. Int J Solids Struct 2006;43:2513–41.
[25] Hashin Z. Viscoelastic behavior of heterogeneous media. J Appl Mech, ASME 1965;32E:630–6.
[26] Masson R, Zaoui A. Self-consistent estimates for the rate-dependent elastoplastic behavior of polycrystalline materials. J Mech Phys Solids 1999;47:1543–68.
[27] Pierad O, Doghri I. An enhanced affine formulation and the corresponding numerical algorithms for the mean-field homogenization of elasto-viscoplastic composites. Int J Plast 2006;22:131–57.
[28] Doghri I, Tinel L. Micromechanics of inelastic composites with misaligned inclusions: numerical treatement of orientation. Comput Methods Appl Mech Eng 2005;195:1387–406.
[29] Nedjar B. An anisotropic viscoelastic fibre-matrix model at finite strains: continuum formulation and computational aspects. Comput Methods Appl Mech Eng 2007;196:1745–59.
[30] Klinkel S, Gavazzi C, Nigam H. Elastoplastic fibre-matrix material model at finite elastic-plastic strains. Comput Mech 2005;35:409–17.
[31] Notta-Cuvier D, Lauro F, Bennani B, Balieu R. An efficient modelling of inelastic composites with misaligned short fibres. Int J Solids Struct 2013;50:2857–71.
[32] Nikolov S, Doghri I, Pierard O, Zealouk L, Goldberg A. Multi-scale constitutive modeling of the small deformations of semi-crystalline polymers. J Mech Physi Solids 2002;50:2275–302.
[33] Ohkami T, Ichikawa Y. A parameter identification procedure for viscoelastic materials. Comput Geotech 1997;21:255–75.
[34] Perzyna P. Fundamental problems in viscoplasticity. Adv Appl Mech 1966;9:243–377.
[35] Raghava R, Caddell RM, Yeh GSY. The macroscopic yield behaviour of polymers. J Mater Sci 1973;8:225–32.
[36] Balieu R, Lauro F, Bennani B, Delille R, Matsumoto T, Mottola E. A full coupled elastoviscoplastic damage model at finite strains for mineral filled semi-crystalline polymer. Int J Plast 2013;51:241–71.
[37] Notta-Cuvier D, Lauro F, Bennani B, Balieu R. Damage of short-fibre reinforced materials with anisotropy induced by complex fibres orientations. Mech Mater 2014;68:193–206.
[38] Notta-Cuvier D, Lauro F, Bennani B. Modelling of progressive fibre/matrix debonding in short-fibre reinforced composites up to failure. Int J Solids Struct 2015;66:140–50.
[39] Bowyer WH, Bader MG. On the re-inforcement of thermoplastics by imperfectly aligned discontinuous fibres. J Mater Sci 1972;7:1315–21.
[40] Wang Yu, Guitino Alberto M. Full-field measurements of heterogeneous deformation patterns on polymeric foams using digital image correlation. Int J Solids Struct 2002;39:3777–96.
[41] Schindelin J, Arganda-Carreras I, Frise E. Fiji: an open-source platform for biological-image analysis. Nat Methods 2012;9(7):676–82.
[42] Thin TBN, Morioka M, Yokoyama A, Hamanaka S, Yamashita K, Noromura C. Measurement of fibre orientation distribution in injection-molded short-glass-fiber composites using X-ray computed tomography. J Mater Process Technol 2015;216:1–9.
[43] Hull D, Clyne TW. An introduction to composite materials. 2nd ed. Cambridge solid state science; 1996. Series.
[44] Thomason JL. Structure-Property relationships in glass-reinforced polyamide, Part 1: the effects of fiber content. Polym Compos 2006;27:552–62.
[45] Thomason JL. Structure-Property relationships in glass-reinforced polyamide, Part 2: the effects of average fiber diameter and diameter distribution. Polym Compos 2007;28:331–43.
[46] Thomason JL. The influence of fibre length, diameter and concentration on the strength and strain to failure of glass fibre-reinforced polyamide 6,6. Compos Part A 2008;39:1618–24.